Control of phase transition patterning in the wake of A + B → C reaction fronts

N. Maton,[1] G. Facchini,[2] and A. De Wit[1]
[1]*Nonlinear Physical Chemistry Unit, CP231, Université libre de Bruxelles (ULB), Boulevard du Triomphe, 1050 Brussels, Belgium*
[2]*Université Paris Cité, CNRS, Matière et Systèmes Complexes, F-75013 Paris, France*

(Received 25 June 2026; accepted 25 September 2026; published 22 October 2026)

When two initially separated reactants A and B are put in contact, a chemical front can develop if a bimolecular A + B → C reaction interplays with diffusion. In the case of a precipitation reaction, a phase transition may occur in the wake of this reaction front provided that the concentration of C is larger than a critical threshold. We analyze the scalings of resulting phase transition patterns in both one-dimensional (1D) and two-dimensional (2D) rectilinear and radial geometries by numerical simulation of the Cahn-Hilliard equation with a reactive source term, solution of reaction-diffusion-advection equations for the concentrations of A and B. We find that the temporal and spatial scalings of the precipitate patterns depend on the properties of the A + B → C fronts and can be controlled by the injection flow rate Q. In particular, we show that the Matalon-Packter law classically used to characterize Liesegang patterns in one-dimensional rectilinear reaction-diffusion systems can be generalized to 1D radial geometry with injection. We discuss the further generalization of pattern selection between stripes and spotted patterns in 2D systems.

DOI: 10.1103/5v7k-w2k3

I. INTRODUCTION

Patterns formed by physical, chemical, biological, or geological processes can sometimes emerge in the wake of a moving front. Such a front is a localized reaction zone traveling in space and time which appears when initially separated reactants come in contact by diffusion [1]. Precipitation patterns forming in the wake of a traveling front are currently attracting growing interest for applications such as CO_2 mineralization [2], growth of self-organized architectures [3–5], separation of metal ions [6], polymorph selection [7,8], microscale stamping [9], or biomorph growth [10], to name a few.

The controlled engineering of such patterns relies on understanding the properties of a phase transition occurring in the wake of a moving front, which is not a trivial task as the morphology of these precipitates can be complex. For example, a mineralization reaction developing within a radial flow in a confined geometry has been shown to produce very complex precipitation patterns of carbonates, the symmetries of which depend on the injection flow rate and on the initial concentrations of the reactants [2,11–13]. Similarly, precipitation in flow conditions of chemical gardens [4], oxalates [7,14], or other products [15,16] can produce a wealth of different chemohydrodynamic structures.

Controlling the properties of such complex phase transition patterning in the wake of advected reaction fronts requires us to understand first the influence of geometry and advection on chemical fronts in the absence of phase transition. In that respect, Brau *et al*. showed recently that, in the case of a radial injection of a reactant A into a pool of reactant B, classical scalings of A + B → C reaction-diffusion fronts [17] are maintained, but the flow affects the prefactors, i.e., modifies the total amount of product generated in space and time and the position of the front, which paves the way to a flow control of the front dynamics [18].

If the reaction takes place in solution and the product C remains liquid, good agreement between the theoretical predictions and experimental results is obtained [18], even though convective effects can perturb the dynamics [19,20]. The next step is then to see how to use these new reaction-diffusion-advection scaling laws to control precipitation patterns.

In the absence of flows, Liesegang structures, i.e., precipitation bands forming in the wake of a reaction-diffusion front, have long been studied [3,21] as they are a promising tool for surface micropatterning and fabrication applications, including microlens arrays and multilevel microfluidic systems [9,22,23]. They are typically obtained when ions diffuse and react through a porous matrix like a gel or a mineral substrate. Experimentally, Liesegang bands have been extensively studied in rectilinear geometries corresponding to the classical cases where one outer electrolyte diffuses inside a gel loaded with the inner electrolyte in a test tube. Different models have been developed and various scaling laws have been found to characterize these rectilinear Liesegang bands [24]. Among the various theoretical approaches, a model coupling a Cahn-Hilliard equation for phase separation to an A + B → C reaction-diffusion front has been shown to reproduce Liesegang bands with their scaling laws in a one-dimensional (1D) rectilinear geometry [25].

In a radial geometry, Liesegang rings with slightly modified scaling laws can also be obtained by the interplay of reaction and diffusion [26,27]. Some results have also been found in a 1D rectilinear geometry where the transport mechanisms of the species are a combination of diffusion and advection [28]. In radial 2D systems, experiments and simulations using a reactive CH model with diffusive transport have shown that rings or spots of precipitates are formed depending on the values of parameters and that the transition threshold, wavelength, and size of the resulting precipitates vary with the initial concentrations of the reactants [27,29].

 ©2026 American Physical Society

However, experimentally, it is difficult to maintain the point source with a constant concentration in the presence of diffusion only in a radial 2D system. Injection of one of the reactants from a point source can maintain this constant concentration at the central boundary, but, to our knowledge, scaling laws have not been generalized to the case where there is both advection and diffusion in a radial geometry.

In this context, we investigate theoretically how precipitation patterns developing in the wake of $A + B \rightarrow C$ fronts can be controlled by varying the initial concentrations of the reactants, the geometry, and the injection flow rate. To do so, we analyze numerical solutions of reaction-diffusion-advection equations for concentrations of reactants A and B coupled to a Cahn-Hilliard (CH) equation, which accounts for the phase transition. We show that the reaction-diffusion (RD) spacing law known for precipitate bands is recovered in a 1D radial geometry with advection. We further show how the Matalon-Packter law can be generalized to this 1D radial case. Finally, we show that the simple scaling law of a 1D radial front allows us to predict the selection of bands or hexagonal precipitate structures in 2D radial flow systems.

The article is organized as follows: First, we introduce the reactive CH model. Second, we summarize what is known about this model as applied to RD Liesegang patterns in rectilinear geometries without any injection. Next, we generalize scalings of the reactive CH model to a radial geometry with injection, assuming invariance in the azimuthal direction. Finally, we release the assumption of radial symmetry and study a full 2D system to explore how varying the injection flow rate and initial concentrations can affect the morphology of the precipitation pattern.

II. REACTIVE CH MODEL

Let us consider a reactor initially filled with species B in which a solution of species A is injected at a constant flow rate Q. Upon contact, A and B produce C following a bimolecular reaction $A + B \rightarrow C$. The product C can precipitate if its concentration is larger than its solubility. The spatial distribution of this precipitate can be described by a phase variable ϕ defined as a linear transformation of the concentration c of species C:

$$\phi = \frac{2c - c_s - c_l}{c_s - c_l}, \tag{1}$$

where c_s is the number of moles of C in a given volume of its solid phase, and c_l is the solubility of C. $\phi = 1$ and -1 correspond then to the solid precipitate phase ($c = c_s$) and to the liquid saturated phase ($c = c_l$), respectively. Assuming that A and B have the same diffusion coefficient, the dimensionless model reads (see Appendix A for the nondimensionalization) [25]

$$\partial_t a + \vec{v} \cdot \vec{\nabla} a = \nabla^2 a - ab, \tag{2}$$

$$\partial_t b + \vec{v} \cdot \vec{\nabla} b = \nabla^2 b - ab, \tag{3}$$

$$\frac{\partial \phi}{\partial t} = -\lambda \nabla^2 (\epsilon \phi - \gamma \phi^3 + \sigma \nabla^2 \phi) + ab. \tag{4}$$

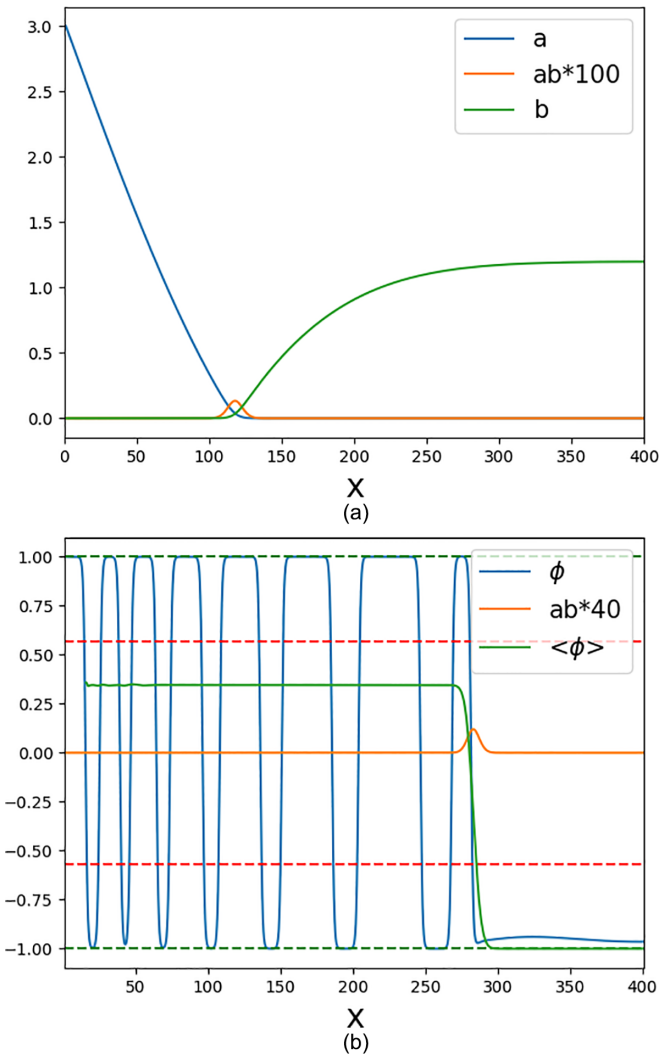

FIG. 1. (a) Reaction-diffusion profiles of the concentration of A, B, and of the reaction rate ab in a bimolecular $A + B \rightarrow C$ front shown at $t = 6000$ for $a_0 = 3$ kept constant at $x = 0$ and $v = 0$, $b_0 = 1$, and hence $\beta = \frac{1}{3}$. The reaction front progresses to the right thanks to the constant feeding of A. (b) Spatial pattern of the phase variable ϕ (in blue) when a phase transition develops in the wake of the reaction front. This occurs when the source term ab (in orange) brings the average value of the phase variable (in green) inside the unstable zone delimitated by $\phi_m^{\pm}$ (red dashed lines). The green dashed lines show the limit of the metastable zone $\phi_s^{\pm}$. Values of parameters are $v = 0$, $b_0 = 1.2$, $\beta = 0.01$, $t = 6000$, $\lambda = 1$.

Equations (2) and (3) are reaction-diffusion-advection (RDA) equations for the dimensionless concentrations a and b of reactants A and B, respectively. The advection speed $\vec{v}$ as well as the initial and boundary conditions will depend on the specific geometry studied. These RDA equations allow us to compute the evolution of the reaction front. When A comes in contact with B, a reaction front forms and moves with time because of reaction, diffusion, and injection. Figure 1(a) shows an example of a front featuring the concentration of A and B and the reaction rate ab in a rectilinear geometry with constant supply of A at the left boundary. The parameters that control the properties of this reaction front are the initial

concentrations a_0 and b_0, and the injection flow rate Q if advection is present.

The Cahn-Hilliard equation (4) describes the phase separation between domains filled with precipitate ($\phi = 1$) and domains in the liquid saturated phase ($\phi = -1$). The source term ab in Eq. (4) corresponds to the production of C and thus the appearance of new precipitate and provides the coupling between the RDA and the CH equations. We make the assumption that C precipitates fast enough so that the displacement caused by the advection when C is still in solution is negligible, i.e., there is no advection term in the CH equation. This is consistent with experimental results in confined geometries, where it has been seen that when C precipitates, it does not move anymore [2,13,18].

The coefficients ϵ and γ determine the two concentrations that minimize the free energy potential as well as the boundaries between the stable, metastable, and unstable regions of the phase variable ϕ. The limits of the metastable regime are given by $\phi_s^{\pm} = \pm\sqrt{\epsilon/\gamma}$. The limits of the spinodal region are $\phi_m^{\pm} = \pm\sqrt{\epsilon/3\gamma}$. Finally, σ quantifies the boundary energy between the two different phases and controls the characteristic wavelength $\lambda_{\max}$ of the phase separation pattern. This wavelength can be predicted by a linear stability analysis around a homogeneous phase ϕ_0 in the spinodal region and is equal to

$$\lambda_{\max} = 2\pi\sqrt{\frac{2\sigma}{\epsilon - 3\gamma\phi_0^2}} = \frac{2\pi}{k_{\max}}, \tag{5}$$

where $k_{\max}$ is the most unstable wave number. The corresponding instability growth rate ω can be estimated as:

$$\omega = \lambda\left[(\epsilon - 3\gamma\phi_0^2)k_{\max}^2 - \sigma k_{\max}^4\right] = \frac{2\pi}{\tau}, \tag{6}$$

where τ is the typical growth time. The characteristic propagation speed s of the precipitation front in a homogeneous phase can be computed as the ratio between the wavelength $\lambda_{\max}$ and the associated growth time τ:

$$s = \lambda\left[\left(\epsilon - 3\gamma\phi_0^2\right)/2\right]^{3/2}\sigma^{-1/2}. \tag{7}$$

In our simulations, we fix $\epsilon = \gamma = \sigma = 1$ such that $\phi_s^{\pm} = \pm 1$ and $\phi_m^{\pm} = \pm\sqrt{1/3}$ and we initialize ϕ as

$$\phi(\vec{r}, t = 0) = -1, \tag{8}$$

which corresponds to the diluted liquid phase of C. The boundary conditions are

$$\vec{n}\cdot\vec{\nabla}\phi = \vec{n}\cdot\vec{\nabla}(\nabla^2)\phi = 0, \tag{9}$$

where $\vec{n}$ is the unit vector normal to the boundary. The first condition is a no-flux condition for ϕ and the second one ensures that the total energy from the minimization of which the CH equation is derived cannot increase with time [30].

As shown in Fig. 1(b) for a semi-infinite rectilinear system, when the reaction front progresses, the average value of the phase variable increases in its wake. Once this value becomes larger than the lower limit ϕ_s^- of the spinodal region, precipitate bands form behind the reaction front. This type of model for front-controlled precipitation has already been studied without advection to model Liesegang patterns [25,27,29]. Below we recall the scaling laws characterizing these 1D rectilinear precipitation patterns before showing how the scalings can be extended to a radial geometry in the general RDA case.

III. 1D RECTILINEAR SYSTEMS

A. Infinite system

Let us first consider a rectilinear geometry and an infinite domain. The species are only transported by diffusion, i.e., we take $\vec{v} = \vec{0}$ in Eqs. (2) and (3). The right half of the domain is initially filled with B at concentration b_0 and the left half with A at concentration a_0:

$$\begin{aligned} a(x, t = 0) &= \begin{cases} a_0 & \text{if } x \leqslant 0 \\ 0 & \text{if } x > 0, \end{cases} \\ b(x, t = 0) &= \begin{cases} 0 & \text{if } x \leqslant 0 \\ b_0 & \text{if } x > 0. \end{cases} \end{aligned} \tag{10}$$

In the case of equal diffusion coefficients, A invades the domain if $a_0 > b_0$ and the front evolution is characterized by well known scaling laws [17]. In the long-time regime, the position x_f of the maximum of the reaction rate scales as $t^{1/2}$, the maximum value of the reaction rate R decreases as $t^{-2/3}$, and the width of the front w expands as $t^{1/6}$ [17]. For $a_0 \neq 1$ (see Appendix B), we have explicitly [17,18]

$$x_f = \alpha_{\text{lin}}(\beta)t^{1/2} = 2\,\text{erf}^{-1}\left(\frac{1-\beta}{1+\beta}\right)t^{1/2}, \tag{11}$$

$$R(x_f, t) = \xi_{\text{lin}}(\beta, b_0)t^{-2/3} = \frac{29}{\pi^4}\left(\frac{b_0 K_{\text{lin}}}{\beta}\right)^{4/3} t^{-2/3}, \tag{12}$$

$$w = \delta_{\text{lin}}(\beta, b_0)t^{1/6} = \pi\left(\frac{b_0 K_{\text{lin}}}{\beta}\right)^{1/3} t^{1/6}, \tag{13}$$

where $\beta = b_0/a_0$ and

$$K_{\text{lin}}(\beta) = \frac{(1+\beta)}{2\sqrt{\pi}}e^{-\alpha_{\text{lin}}^2/4}. \tag{14}$$

B. Amount of product in the wake of the rectilinear front

Antal *et al.* have shown that, for this 1D infinite system, precipitate bands form when the reaction front generates enough product for ϕ to reach locally the spinodal region threshold but not enough to obtain continuous precipitation [25]. The total amount of product n_c can be computed as [31]

$$n_c = a_0\frac{58}{\pi^3}\eta_{\text{lin}}K_{\text{lin}}S_{\text{lin}}t^{1/2}, \tag{15}$$

where η_{lin} is a constant related to the specific shape of the reaction front and S_{lin} is the dimensionless area of the contact zone transverse to the direction of propagation. To compute the total amount of product per unit volume generated in the wake of the moving front, we divide that expression by $S_{\text{lin}}\,x_f$, where x_f is the position of the maximum reaction rate and get the following expression for the average concentration $\langle c_{\text{lin}}\rangle$ of the product left behind the front:

$$\langle c_{\text{lin}}\rangle(b_0, \beta) = a_0\frac{58}{\pi^3}\frac{\eta_{\text{lin}}K_{\text{lin}}(\beta)}{\alpha_{\text{lin}}(\beta)} = \frac{b_0}{\beta}\frac{58}{\pi^3}\frac{\eta_{\text{lin}}K_{\text{lin}}(\beta)}{\alpha_{\text{lin}}(\beta)}. \tag{16}$$

From this expression and using the definition (1) of the phase variable, we can deduce the average value $\langle\phi_{\text{lin}}\rangle$ of the phase

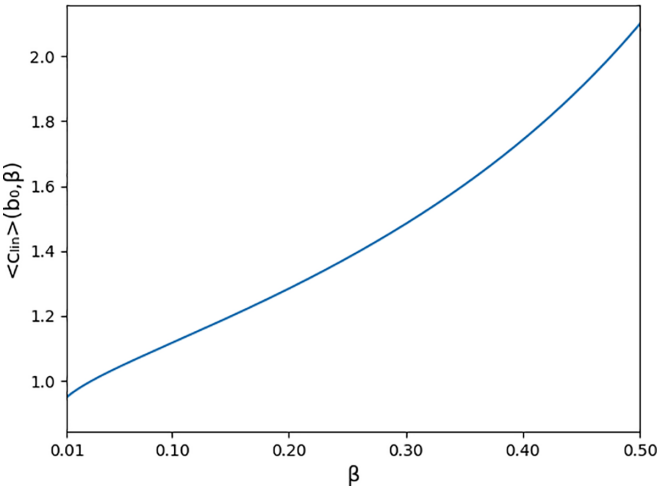

FIG. 2. Average amount $\langle c_{\text{lin}} \rangle$ of product generated in the wake of the front as a function of β with $\eta_{\text{lin}} * b_0 = 0.25$.

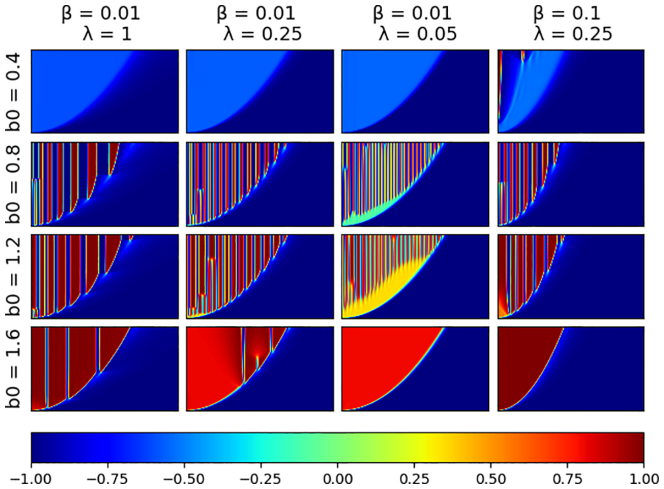

FIG. 3. Space-time maps of ϕ in a semi-infinite rectilinear system for $\vec{v} = 0$, and variable b_0, β and λ when a_0 is kept fixed at the left boundary. The vertical axis corresponds to time $t \in [0, 6000]$ running upwards and the horizontal axis represents $x \in [0, 400]$.

variable left in the wake of the front:

$$\langle \phi_{\text{lin}} \rangle = \phi_0 + \langle c_{\text{lin}} \rangle. \tag{17}$$

Controlling the ratio β of the initial concentrations of the reactants and their absolute values, we can thus control the average value $\langle \phi_{\text{lin}} \rangle$ of the phase variable behind the front. Equation (16) shows that, for a fixed value of β, $\langle c_{\text{lin}} \rangle \propto a_0$, i.e., more product is logically generated when the absolute values of the concentrations increase. However, for a fixed value of b_0, $\langle c_{\text{lin}} \rangle$ and thus $\langle \phi_{\text{lin}} \rangle$ are larger when β increases (see Fig. 2). This means, for instance, that increasing a_0 while keeping b_0 constant decreases β. The average amount of product generated decreases then because the reaction front moves faster.

Precipitation occurs if $\langle \phi_{\text{lin}} \rangle$ is larger than the spinodal threshold ϕ_m^-. The precipitation front is either slaved to the reaction front or lags behind it, depending on the value of the mobility λ in the CH equation. If the CH instability front is enslaved to the reaction front, the resulting bands of precipitate obey the scaling laws characteristic of Liesegang patterns [25]. The time law states that the position x_n of the nth band is proportional to $\sqrt{t_n}$, where t_n is the time at which the nth band appears. This is a direct consequence of the diffusive motion of the front characterized by Eq. (11). The spacing law states that, for large n, the ratio of the positions of two consecutive bands approaches a constant value, i.e.,

$$\frac{x_n}{x_{n-1}} \longrightarrow 1 + p, \tag{18}$$

where p is the spacing coefficient that depends on the concentrations a_0 and b_0 of the outer and inner reactants following Matalon-Packter law:

$$p = F(b_0) + G(b_0)\beta, \tag{19}$$

where F and G are decreasing functions of their arguments.

C. Semi-infinite system

Let us now consider a semi-infinite rectilinear RD system with no injection with a boundary at the position $x = 0$ where the concentration a_0 of reactant A is kept constant. Figure 3 shows spatiotemporal maps of ϕ obtained by solving Eqs. (2)–(4) with $\vec{v} = 0$ on an equivalent finite 1D rectilinear domain of length L with the initial conditions

$$\begin{aligned} a(x, t = 0) &= 0, \\ b(x, t = 0) &= b_0 \end{aligned} \tag{20}$$

and boundary conditions

$$\begin{aligned} a(x = 0, t) &= a_0, \quad \frac{\partial a}{\partial x}(x = L, t) = 0, \\ b(x = 0, t) &= 0, \quad \frac{\partial b}{\partial x}(x = L, t) = 0. \end{aligned} \tag{21}$$

As the system is constantly fed with reactant A, the front will always invade the reactant B, whatever the value of β. The diffusive transport translates into the characteristic $x \propto \sqrt{t}$ shape of the front progression in space-time maps of the dynamics (Fig. 3). We see that, for a given value of β, the amount of product generated increases with b_0, allowing us to switch from a homogeneous liquid phase (in blue) to bands of precipitate (in red) once the average value of ϕ left behind the reaction front, $\langle \phi_{\text{lin}}^{\text{si}} \rangle$ (given in Appendix C), is large enough, i.e., exceeds the unstable threshold ϕ_m^-.

For a fixed value of b_0, an increase of β (corresponding to a decrease of a_0) implies that the front slows down, more product accumulates on a smaller region and thus $\langle \phi_{\text{lin}}^{\text{si}} \rangle$ increases. In some cases, $\langle \phi_{\text{lin}}^{\text{si}} \rangle$ can even exceed the ϕ_m^+ upper boundary of the unstable region such that a homogeneous solid phase (in red) is obtained.

In the presence of precipitation, we can distinguish two cases, depending on the value of λ and the mobility of the phase variable. For $\lambda = 1$, the precipitation front is slaved to the reaction front. Over the course of time, both the distance between consecutive bands and their width increase, in agreement with classical behavior of Liesegang patterns [25]. However, if λ becomes too small (see the $\lambda = 0.05$ cases on Fig. 3, for instance), the precipitation front lags behind the

reaction front and successively invades the system as a perturbation in a supercritical zone. The precipitation front travels then at constant speed and the wavelength of the pattern is approximately constant, until it catches the RD front. Note that the speed s of the CH instability in a homogeneous phase is constant [Eq. (7)] [32] while the speed of the reaction front decreases as $t^{-1/2}$, so in practice the precipitation front will always catch up the reaction front and become enslaved to it at some time.

IV. RADIAL GEOMETRY WITH INJECTION

Let us now explore the radial case which is more relevant in Nature [33,34] and for industrial applications [24,35,36]. We will consider in addition a radial injection speed imposed by a constant flow rate, i.e. $v_r = Q/r$. We will show here that the flow rate can control the properties of the precipitation bands and that scaling laws of Liesegang bands can be generalized to the radial flow geometry. To do so, we first assume radial symmetry of the phase variable such that we can neglect the dependence in the azimuthal coordinate. The reactive CH model [(2)–(4)] can then be expressed in polar coordinates as

$$\frac{\partial a}{\partial t} + \frac{Q}{r}\frac{\partial a}{\partial r} = \frac{\partial^2 a}{\partial r^2} + \frac{1}{r}\frac{\partial a}{\partial r} - ab, \tag{22}$$

$$\frac{\partial b}{\partial t} + \frac{Q}{r}\frac{\partial b}{\partial r} = \frac{\partial^2 b}{\partial r^2} + \frac{1}{r}\frac{\partial b}{\partial r} - ab, \tag{23}$$

$$\frac{\partial \phi}{\partial t} = -\lambda\nabla^2[(\epsilon\phi - \gamma\phi^3 + \sigma\nabla^2\phi)] + ab. \tag{24}$$

where $\nabla^2 = \frac{\partial^2}{\partial r^2} + \frac{1}{r}\frac{\partial}{\partial r}$. The initial and boundary conditions are

$$\begin{aligned} a(r > r_0, t = 0) &= 0, \\ b(r > r_0, t = 0) &= b_0, \end{aligned} \tag{25}$$

where r_0 is a small radius introduced to avoid singularity at $r = 0$. The boundary conditions are

$$\begin{aligned} a(r = r_0, t) &= a_0, \quad \frac{\partial a}{\partial r}(r = R_{\text{tot}}, t) = 0, \\ b(r = r_0, t) &= 0, \quad \frac{\partial b}{\partial r}(r = R_{\text{tot}}, t) = 0, \end{aligned} \tag{26}$$

where R_{tot} is the radius of the domain.

In these conditions, it has been shown that the front position r_f, the reaction rate maximum $R(r_f, t)$, and the width w of the front governed by reaction-diffusion-advection equations obey temporal scaling laws in the long-time regime which are similar to the scaling laws [(11)–(13)] of the rectilinear RD front [18]. However, the coefficients are now function also of the flow rate Q as

$$r_f = \alpha_{\text{rad}}(\beta, Q)t^{1/2} = 2\kappa(Q, \beta)^{1/2}t^{1/2}, \tag{27}$$

$$R = \xi_{\text{rad}}(\beta, b_0, Q)t^{-2/3} = \frac{29}{\pi^4}\left(\frac{b_0 K_{\text{rad}}}{\beta}\right)^{4/3} t^{-2/3}, \tag{28}$$

$$w = \delta_{\text{rad}}(\beta, b_0, Q)t^{\frac{1}{6}} = \pi\left(\frac{b_0 K_{\text{rad}}}{\beta}\right)^{-1/3} t^{1/6}, \tag{29}$$

with

$$\kappa(Q, \beta) = \chi^{-1}\left(\frac{Q}{2}, \frac{\beta}{1+\beta}\right), \tag{30}$$

where $\chi(x, y) = \Gamma(x, y)/\Gamma(0, x)$ and $\Gamma(x, y)$ are the upper regularized incomplete, and incomplete gamma functions, respectively, and K_{rad} is defined by

$$K_{\text{rad}}(Q, \beta) = \frac{(1+\beta)}{\Gamma(0, Q/2)}\kappa^{(Q-1)/2}e^{-\kappa}. \tag{31}$$

Note that, if $Q = 1$, the terms proportional to $1/r$ in Eqs. (22) and (23) cancel out, and we recover the specific semi-infinite rectilinear equations for a and b similar to the one studied in Fig. 1 (see details and scalings of the semi-infinite case in Appendix C).

A. Amount of product in the wake of the radial front

The total amount ρ of product left behind the front is given by [31]

$$\rho = 2\pi h\eta_{\text{rad}}\alpha_{\text{rad}}\xi_{\text{rad}}\delta_{\text{rad}}t, \tag{32}$$

where h is the height of the reactor and η_{rad} is a constant related to the specific shape of the reaction front. As in the rectilinear case, we can divide this expression by the volume $\pi h r_f^2$ spanned by the front to obtain the average amount of C produced per unit volume behind the front:

$$\begin{aligned} \langle c_{\text{rad}}\rangle &= \frac{2\eta_{\text{rad}}\alpha_{\text{rad}}\xi_{\text{rad}}\delta_{\text{rad}}t}{\alpha_{\text{rad}}^2 t} \\ &= a_0\frac{29}{\pi^3}\frac{\eta_{\text{rad}}K_{\text{rad}}}{\kappa^{1/2}} = \frac{b_0}{\beta}\frac{29}{\pi^3}\frac{\eta_{\text{rad}}K_{\text{rad}}}{\kappa^{1/2}}. \end{aligned} \tag{33}$$

From this expression, we can deduce the average value $\langle\phi_{\text{rad}}\rangle$ of the phase variable left behind the reaction front as

$$\langle\phi_{\text{rad}}\rangle = \phi_0 + \langle c_{\text{rad}}\rangle. \tag{34}$$

In Fig. 4, we compare the flow rate dependence of the analytical value of $\langle\phi_{\text{rad}}\rangle$ computed by Eq.(34) to its numerical value measured behind the reaction front. An excellent agreement is obtained. Some slight discrepancy is observed at the lowest values of Q because, when the flow rate is small, the reaction front is slow and, hence, some product can diffuse ahead of the reaction front.

Analysis of the parameter dependence of $\langle\phi_{\text{rad}}\rangle$ given by Eqs. (33) and (34) shows that, for a fixed value of Q, precipitation is favored when increasing the absolute values of the reactant concentrations a_0 and b_0 at constant β. For a fixed initial concentration of B, precipitation can be obtained by decreasing the concentration a_0 of the injected solution of A, i.e., by increasing β. These trends are the same as in 1D rectilinear systems without injection, as shown in Fig. 3. We recall that this specific rectilinear RD front obeys the (a_0, β) parameter dependence given by Eqs. (27)–(29) for the specific value $Q = 1$. The only small discrepancies between simulations of Fig. 2 in rectilinear coordinates and simulations using model (22)–(24) for $Q = 1$ in polar coordinates is, in the radial case, a slight inward drift of bands close to the injection point due to curvature effects induced by the $1/r$ terms in the CH equation. Indeed, while Eqs. (22) and (23) are identical to those in rectilinear geometries for $Q = 1$, the $1/r$ terms

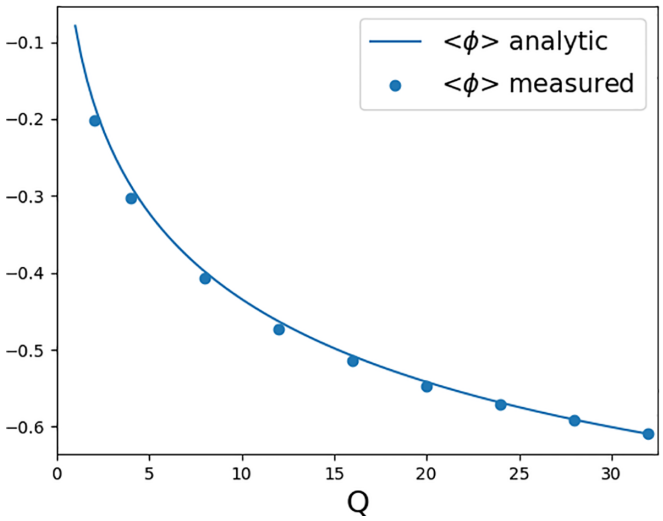

FIG. 4. Comparison of the analytic average value $\langle\phi_{\rm rad}\rangle$ given by Eq. (34) with the average value $\langle\phi\rangle$ computed behind the reaction front in numerical solutions of the reactive CH model at $t = 6000$ in a radial geometry. Parameters are $b_0 = 0.85$, $\beta = 1$, $\lambda = 1$.

in the CH Eq. (24) do not cancel out and are operational to affect the bands close to the injection point where curvature is maximum, as seen in Fig. 5 featuring space-time maps of the phase variable for different values of b_0 and Q for $\beta = 0.01$ and $\lambda = 1$.

B. Effect of advection on precipitation fronts

The novelty in the radial case with injection is that the reaction front can be controlled by the flow rate Q [18]. Here, increasing Q while the other parameters are fixed decreases $\langle\phi_{\rm rad}\rangle$ (see Fig. 4) because the front speed is increased, and consequently the amount of product per unit volume left in the wake of the front is decreased. The advected front travels faster, there are more and more thinner bands, and the distance between them increases (Fig. 5). Above a given flow rate, $\langle\phi_{\rm rad}\rangle$ can become smaller than ϕ_s^-. Radial advection can

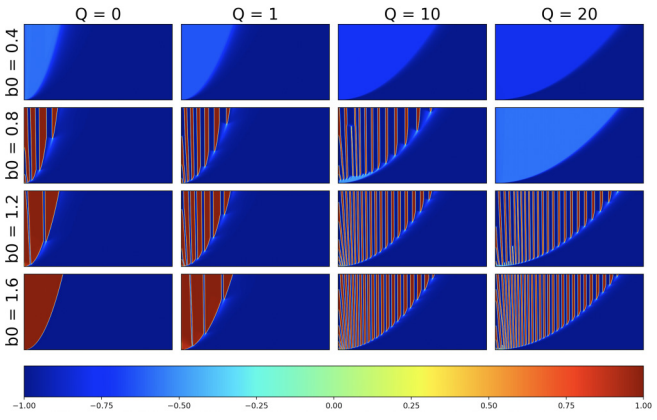

FIG. 5. Space-time map of ϕ in a radial geometry as a function of Q and b_0 for $\beta = 0.01, \lambda = 1$. The vertical axis corresponds to the time $t \in [0, 6000]$ running upwards and the horizontal axis represents $r \in [1, 800]$.

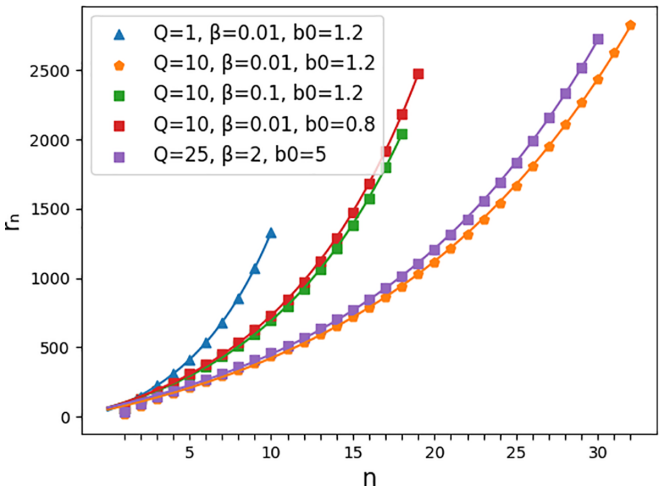

FIG. 6. Position r_n of the nth band as a function of n. Solid curves correspond to the fit by a spacing law $r_n = D\exp(\tilde{p}n - 1)$ for variable values of Q, b_0, and β at $\lambda = 1$.

thus suppress precipitation if it becomes too strong as seen in Fig. 5.

We also see that, as mentioned above, the dynamics at $Q = 1$ is the same as in the rectilinear case (compare with the first column of Fig. 3 shown on a smaller time domain) except for the inward drift of the innermost bands because of curvature effects at small radius. The simulation at $Q = 0$ allows us to extract the pure effect of geometry in the RD case without injection. The outward radial diffusion of A dilutes it while the inward diffusion of B is focusing it more than in a rectilinear case. This imbalance of diffusive fluxes due to geometry tends to slow down the radial front compared to the rectilinear case and, consequently, $\langle\phi_{\rm rad}\rangle$ increases. This explains why at $Q = 0$, $b_0 = 1.6$, $\lambda = 1$, and $\beta = 0.01$, we reach the homogeneous precipitate state for the radial case (Fig. 5) while we are still in the spinodal region in the rectilinear case (Fig. 3).

C. Liesegang scalings

Note that, as in the 1D purely diffusive case, the position r_f of the RDA radial front scales as $\sqrt{t}$ [Eq. (27)], which suggests that the time law of Liesegang bands can be generalized to the radial case. This is also in agreement with Fig. 5, where we see that the spacing between Liesegang bands progressively increases in space and time similarly to the 1D rectilinear diffusive case (Fig. 3). Moreover, far from the center, curvature effects are negligible, the bands become stationary, and we recover a classical spacing law

$$\frac{r_n}{r_{n-1}} \longrightarrow 1 + p. \tag{35}$$

In Fig. 6 we show that the position r_n of the nth ring is well fitted by the form $r_n = D\exp(\tilde{p}n - 1)$, which means that the spacing law is verified with a spacing coefficient $1 + p = \exp(\tilde{p})$. In the same figure, we also show that increasing b_0 while keeping Q and β constant decreases p. This can be understood by the fact that increasing b_0 keeping all other parameters constant induces the formation of more product, thus reducing the distance between precipitation bands.

Conversely, increasing Q while keeping other parameters constant both decreases $\langle\phi_{\rm rad}\rangle$ and increases the front speed, which turns into a decrease of the spacing coefficient p.

D. Matalon-Packter law in the radial case

As the classical spacing law of the rectilinear cases are also recovered in the radial advective case, it is natural to wonder whether the Matalon-Packter law (19) verified for rectilinear RD systems can also be generalized to the radial geometry with injection. In the rectilinear case, the physical understanding of how the spacing coefficient p varies with β and b_0 boils down to understanding how precipitation patterns depend on the speed of the reaction front and the amount of product generated. First, at fixed values of β (i.e., at a given constant front speed), increasing the absolute values of concentrations decreases the spacing p as $F(b_0)$ and $G(b_0)$ in (19) are decreasing functions of b_0. This can be connected to the fact that the amount of product generated is then larger (i.e. $\langle\phi_{\rm lin}\rangle$ increases) and we need to travel a smaller distance before precipitation occurs again. Second, when b_0 is fixed, the spacing p is an increasing function of the ratio of initial concentration $\beta = b_0/a_0$, i.e., a decreasing function of the speed. This means that decreasing a_0 at fixed b_0 leads to more spaced precipitation bands. This is logically connected to the fact that the front speed is then slower and precipitation bands have more time to thicken before the next band appears. Phrased differently, the larger β at fixed b_0 is, the slower is the front speed and the larger is p.

With this understanding in mind, we now turn to the radially advected case wondering how the introduction of the new parameter that is the flow rate Q can alter this picture. Intuitively, the advective case must consider new effective variables which combine Q, b_0, and β because the amount of precipitate and the front speed now depend on these three variables in a nontrivial way. We then propose an effective Matalon-Packter law of the form

$$p = H(b_{0\rm eq}) + J(b_{0\rm eq})\beta_{\rm eq}, \tag{36}$$

where now $b_{0\rm eq}$ and $\beta_{\rm eq}$ are not only functions of β and b_0 but, most importantly, can be controlled by the flow rate Q. We assume that H and J are decreasing functions of their argument $b_{0\rm eq}$ that controls the total amount of product generated for a given front speed while $\beta_{\rm eq}$ addresses the parameter dependence of p on the front speed. With this picture in mind, given a set of Q, β, and b_0 and the corresponding radial front, we define $\beta_{\rm eq}$ as the value of β that would yield the same front velocity in a rectilinear case without advection. Analogously, for this given speed, $b_{0\rm eq}(b_0, \beta, Q)$ would be the initial concentration of b necessary to produce the same averaged amount of ϕ in a rectilinear case. To formalize this equivalence, we impose that x_f given by (11) is equal to r_f given by (27), which gives $\alpha_{\rm lin}(\beta_{\rm eq}) = \alpha_{\rm rad}(Q, \beta)$ and leads to

$$2\,\mathrm{erf}^{-1}\left(\frac{1-\beta_{\rm eq}}{1+\beta_{\rm eq}}\right) = 2\kappa^{1/2}(Q,\beta), \tag{37}$$

and thus

$$\beta_{\rm eq}(Q,\beta) = \frac{1-\mathrm{erf}[\kappa^{1/2}(Q,\beta)]}{1+\mathrm{erf}[\kappa^{1/2}(Q,\beta)]}. \tag{38}$$

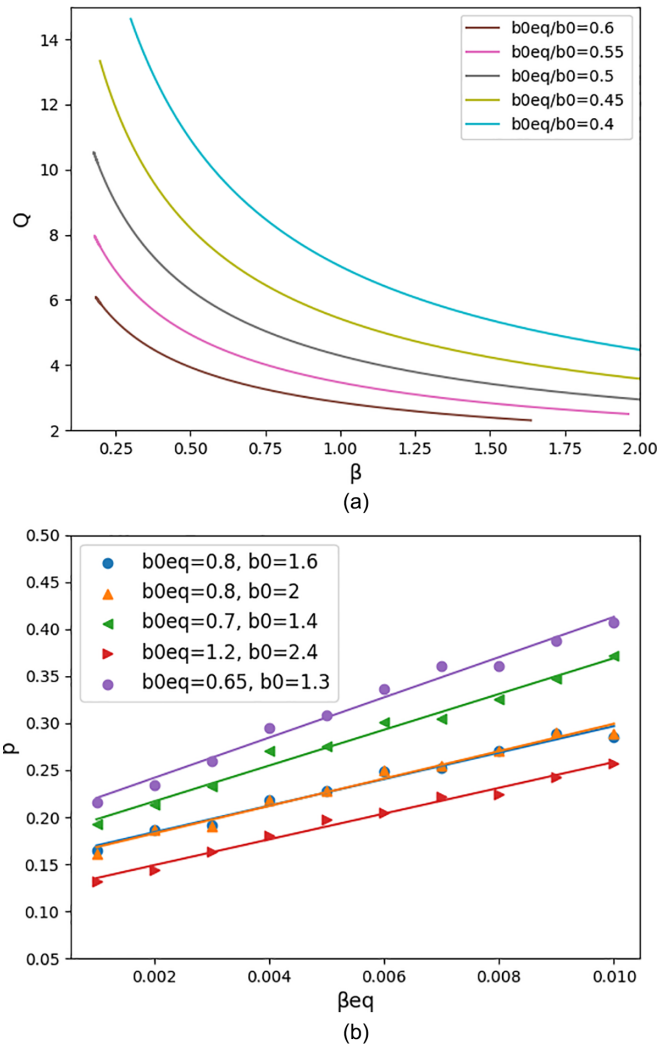

FIG. 7. (a) Curves in the (Q, β) parameter plane for which $b_{0\rm eq}/b_0$ is a constant. (b) Spacing coefficients p as a function of $\beta_{\rm eq}$ while keeping $b_{0\rm eq}$ constant and $\lambda = 1$ using values of Q and β on curves $b_{0\rm eq}/b_0 = 0.5$ or 0.4. Straight lines coincide with the linear fit of the generalized Matalon-Packter law in Eq. (36).

Next, we impose that the amount of product generated in the rectilinear case given by Eq. (16) is equal to that obtained in the radially advected case given by Eq. (33), that is $\langle c_{\rm lin}(b_{0\rm eq}, \beta_{\rm eq})\rangle = \langle c_{\rm rad}(b_0, \beta, Q)\rangle$, which gives

$$a_{0\rm eq}\frac{29}{\pi^3}\frac{\eta_{\rm lin}K_{\rm lin}(\beta_{\rm eq})}{\mathrm{erf}^{-1}\left(\frac{1-\beta_{\rm eq}}{1+\beta_{\rm eq}}\right)} = a_0\frac{29}{\pi^3}\frac{\eta_{\rm rad}K_{\rm rad}(Q,\beta)}{\kappa^{1/2}(Q,\beta)}, \tag{39}$$

where $a_{0\rm eq} = b_{0\rm eq}/\beta_{\rm eq}$ and $a_0 = b_0/\beta$. The final expression reads

$$b_{0\rm eq}(Q,\beta,b_0) = b_0 * \frac{\eta_{\rm rad}}{\eta_{\rm lin}}\frac{\beta_{\rm eq}}{\beta}\frac{K_{\rm rad}(Q,\beta)}{K_{\rm lin(\beta_{eq})}} * \frac{\mathrm{erf}^{-1}\left(\frac{1-\beta_{\rm eq}}{1+\beta_{\rm eq}}\right)}{\kappa^{1/2}(Q,\beta)}. \tag{40}$$

In the following, $\eta_{\rm rad}/\eta_{\rm lin}$ is approximated by 1 [31]. Then, if our ansatz in Eq. (36) is correct, p should depend linearly on $\beta_{\rm eq}$ if Q and β are varied while keeping $b_{0\rm eq}$ constant. To explain this constraint, we have reported in Fig. 7(a) how Q

must vary as a function of β to keep the ratio $b_{0\mathrm{eq}}/b_0$ constant. In Fig. 7(b), $p = f(\beta_{\mathrm{eq}})$ is measured from simulations with values of Q and β taken from a curve where $\frac{b_{0\mathrm{eq}}}{b_0}$ is constant. We see that there is a linear dependence with a slope that is a decreasing function of $b_{0\mathrm{eq}}$, which means that the modified Matalon-Packter law (36) is verified. This new relation gives the explicit dependence of the spacing coefficient p on the flow rate Q and β in the radially advected case.

V. 2D RADIAL GEOMETRY WITH INJECTION

Eventually, we explore what happens when the assumption of radial symmetry is released. Bifurcation diagrams of 2D solutions of the nonreactive Cahn-Hilliard equation, i.e., with no source term, in homogeneous conditions show that, depending on the average value $\langle\phi_{\mathrm{rad}}\rangle$ of the phase variable and on the periodicity of the precipitate patterns, bands or spots minimize the total energy of the system [37]. Close to the spinodal line, for a fixed wavelength, spots of precipitates in hexagonal symmetry are the only stable structure. Close to $\langle\phi_{\mathrm{rad}}\rangle = 0$, bands of precipitate are favored. For the reactive CH system and in experiments of precipitation behind a reaction front, Dayeh *et al.* [27] as well as Papp *et al.* [29] have shown that precipitates can self-organize both as spots with hexagonal geometry and as rings.

Here, we will show how, in the reactive system, tuning the injection rate and the initial concentrations of reactants can select either spot or band precipitation patterns. Indeed, as the value of the parameters Q, b_0, and β control the value of $\langle\phi_{\mathrm{rad}}\rangle$ left in the wake of the reaction front, they control the location of the system in the bifurcation diagram. To analyze this pattern selection in radial 2D systems with injection, we solve Eqs. (22)–(24) numerically using the commercial package COMSOL and a backward differentiation scheme with a maximum grid size of 0.15 and a maximum time step of 0.1. The inlet radius is 20 and the outlet radius is 200. The maximum time is 600 with an initial noise term added on ϕ. This noise is a Gaussian noise with amplitude 0.01 everywhere on the domain. Note that, as shown previously [13], the Cahn-Hilliard patterns may exhibit some sensitivity to the spatial discretization, but the pattern selection (i.e., spots versus stripes) and the typical pattern wavelength are preserved upon grid refinement. Here, the results have been checked to be robust with regard to further refinement of the space and time steps. However, spot location can change as it depends on the initial noise seeding the pattern, which is grid-dependent. As an example, Fig. 8 shows that either rings or spots of precipitate or a mixture of both can be obtained starting from the same initial concentrations of the reactants but injecting reactant A with different values of the flow rate Q. Fixing $b_0 = 0.875$ and $\beta = 0.01$ (horizontal dashed line in the lower panel of Fig. 8), we see that, for $Q = 2$, the precipitate self-organizes into concentric rings because $\langle\phi_{\mathrm{rad}}\rangle$ is close to the center of the spinodal region where bands are favored [Fig. 8(a)]. Along a radial cross section of such rings, the solution is similar to the one computed in the radial 1D model. If we increase the flow rate to $Q = 10$, $\langle\phi_{\mathrm{rad}}\rangle$ decreases as the front moves faster, bringing the system closer to the metastable limit where the precipitate self-organizes into spots with hexagonal symmetry and defects in the center due to coarsening [Fig. 8(c)]. In between, i.e., for $Q = 7$ here, a structure where rings transition to spots can be observed [Fig. 8(b)].

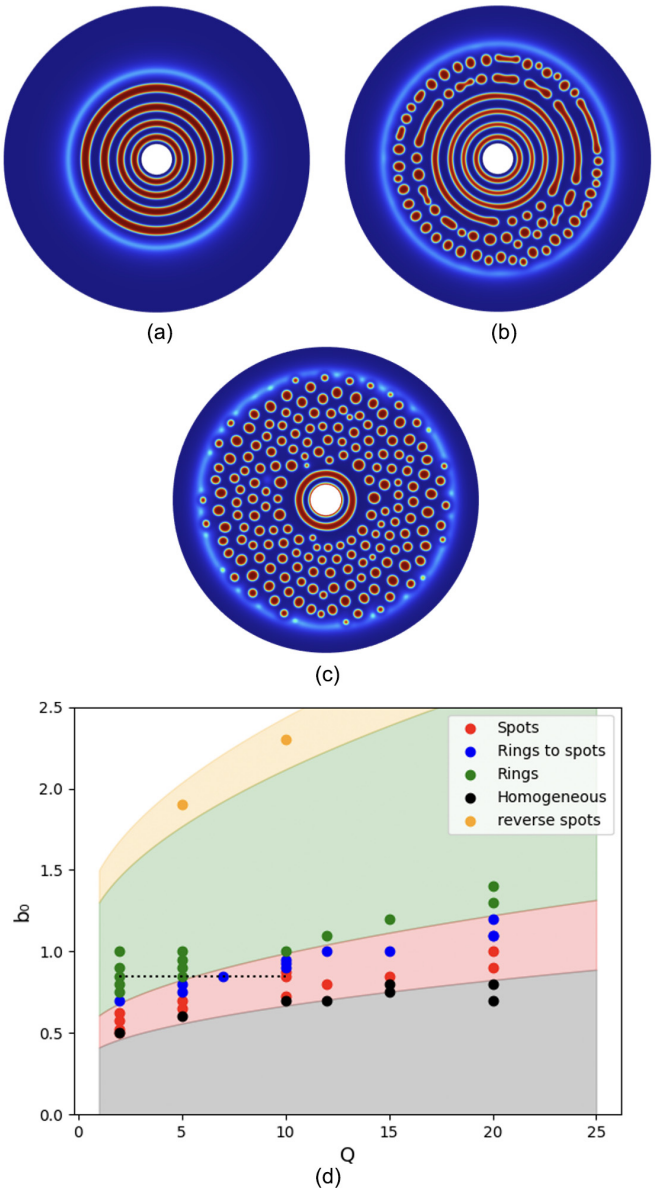

FIG. 8. 2D map of ϕ for $b_0 = 0.875$, $\beta = 0.01$ at time $t = 600$ and (a) $Q = 2$, (b) $Q = 7$, and (c) $Q = 10$ with a colormap between blue ($\phi = -1$) and red ($\phi = 1$). (d) Symmetry of the precipitate pattern in a 2D radial geometry in the parameter space spanned by the initial concentration b_0 and the injection flow rate Q for $\beta = 0.01$, $\lambda = 1$. Starting from a perturbed homogeneous state where $\phi = \langle\phi_{\mathrm{rad}}(b_0, \beta, Q)\rangle$, we switch from no instability in the gray zone to spots of precipitate in the pink zone, bands of precipitate in the green part, and reverse spots of liquid in the yellow zone. The dashed line shows the progression of patterns from panels (a)–(c).

The lower panel of Fig. 8 summarizes the patterns obtained in the parameter space spanned by the initial concentration b_0 of reactant B and the flow rate Q at a fixed arbitrary time $t = 600$. The different colored zones between patterns of different symmetries feature the predictions of the expected pattern obtained by computing $\langle\phi_{\mathrm{rad}}(b_0, \beta, Q)\rangle$ using Eq. (34).

The boundaries drawn to guide the eye have been obtained by running simulations of the nonreactive CH starting from an initial value of the phase $\phi_0 = \langle\phi_{\rm rad}(b_0, \beta, Q)\rangle$. As an example, the pink zone is the range of values of b_0 and Q for which the average of the phase variable $\langle\phi_{\rm rad}(b_0, \beta, Q)\rangle$ that is left behind the reaction front gives spots of $\phi = 1$ in a $\phi = -1$ background in simulations of a nonreactive homogeneous system starting from $\phi_0 = \langle\phi_{\rm rad}(b_0, \beta, Q)\rangle$. The yellow zone represents the zone where we would get reverse spots of the diluted phase $\phi = -1$ in a $\phi = 1$ background. In between, the green zone gathers the parameter space region where simulations in homogeneous conditions feature ring patterns while no precipitation is expected in the gray zone.

The circles on Fig. 8 correspond to the patterns observed in nonhomogeneous conditions when the patterns are triggered in the wake of the moving reaction front. We see that the theoretical predictions based on the computation of $\langle\phi_{\rm rad}(b_0, \beta, Q)\rangle$ by formula (34) in the simplified hypothesis of radial symmetry provide a reliable understanding of the influence of the flow rate Q on pattern selection in fully 2D simulations. At a fixed value of Q, we observe a transition from no precipitation to spots, a mixture of bands and spots, followed by a large zone where only rings are obtained. Reverse spots can only be obtained at much larger concentrations. Most interestingly, if concentrations are fixed, a gradual increase of the flow rate allows us to transition from rings to a mixture of spots and rings, and eventually to only spots. These results pave the way to controlling these various patterns experimentally in flow conditions.

VI. CONCLUSION

Patterns developing in the wake of moving $A + B \to C$ reaction fronts can produce a wealth of different precipitation structures when the product C is a solid phase. We have studied here the properties of such front-driven precipitation patterns by analyzing theoretically the solutions of a reactive Cahn-Hilliard model in both rectilinear reaction-diffusion and radial reaction-diffusion-advection systems. We show that precipitation patterns occur when the average amount of the product of the reaction reaches a given critical value. We have derived analytical expressions showing how this amount is controlled by the initial concentrations of the reactants and their ratio, and by the flow rate in presence of injection. We see that the faster the $A + B \to C$ front is, the less product is generated per unit volume behind the front and hence the less favorable is the phase transition. This can be obtained, for instance, by increasing a_0 or decreasing b_0 at constant β or by increasing the injection flow rate Q for given concentrations. We have further shown that the Matalon-Packter law characterizing RD Liesegang rings spacing can be generalized to the radial geometry with injection modulo a proper definition of new effective variables that control the front dynamics and the amount of precipitate. The new scalings have been confirmed by numerical simulations of the reactive CH model. Finally, we have shown that our simplified 1D approach can be used to predict precipitate pattern selection in 2D radial systems with injection, i.e., whether bands or hexagons are obtained depending on the value of concentrations and injection flow rate. This confirms that advection is a useful tool to control pattern formation in the wake of reaction fronts, and it paves the way to the engineering of flow-controlled new materials.

ACKNOWLEDGMENTS

We thank M. Götzen for preliminary simulations and F. Brau for fruitful discussions. N.M. acknowledges financial support from the F.R.I.A. A.D. thanks the FRS-FNRS for financial support under the PDR "PHYLLO" programme.

DATA AVAILABILITY

There are no publicly available research data or software supporting this manuscript. Requests for further information or data should be sent to the authors.

APPENDIX A: NONDIMENSIONALIZED SYSTEM OF EQUATIONS

Consider a two-dimensional system in which a solution of species A is injected at a constant flow rate Q into a domain initially filled with species B. Upon contact, A and B react to produce C following a bimolecular reaction $A + B \to C$. The product C can precipitate if its concentration is larger than the solubility c_l. The phase of C is described by a phase variable $\phi' = 2c' - c'_s - c'_l$, where c' is the concentration of C and c'_s its concentration in the precipitate. The RDA equations for the dimensional concentrations a', b' of reactants A and B are then coupled to the CH equation with a source term as

$$\begin{aligned}
\frac{\partial a'}{\partial t'} + \vec{v}' \cdot \nabla' a' &= D_A \nabla^2 a' - k a' b', \\
\frac{\partial b'}{\partial t'} + \vec{v}' \cdot \nabla' b' &= D_B \nabla^2 b' - k a' b', \\
\frac{\partial \phi'}{\partial t'} &= -\lambda' \nabla'^2 (\epsilon' \phi' - \gamma' \phi'^3 + \sigma' \nabla'^2 \phi') + k a' b',
\end{aligned} \tag{A1}$$

where D_A and D_B are the diffusion coefficients of A and B, k is the reaction rate, and $\vec{v}'$ is the advection speed. λ', ϵ', γ', and σ' are the dimensional parameters of the CH equation.

To nondimensionalize these equations, we introduce characteristic variables : concentration $c_r = c_s - c_l$, time $\tau = (k c_r)^{-1}$, length $l = \sqrt{D_A \tau}$. The dimensionless variables and parameters are then defined as $t = \frac{t'}{\tau}$, $r = \frac{r'}{l}$ and thus $\nabla = \nabla' * l$, $\delta_B = \frac{D_B}{D_A}$, $A = \frac{a'}{c_r}$, $b = \frac{b'}{c_r}$, $v = \frac{v'\tau}{l}$, $\phi = \frac{\phi'}{c_r}$, $\lambda = \frac{\lambda'}{\tau D_A}$, $\epsilon = \epsilon'$, $\gamma = \gamma' * c_r^2$, $\sigma = \frac{\sigma'}{\tau D_A}$. Multiplying all the dimensional equations by τ / c_r, we get the following dimentionless model:

$$\begin{aligned}
\partial_t a + \vec{v} \cdot \nabla a &= \nabla^2 a - ab, \\
\partial_t b + \vec{v} \cdot \nabla b &= \delta_B \nabla^2 b - ab, \\
\frac{\partial \phi}{\partial t} &= -\lambda \nabla^2 (\epsilon \phi - \gamma \phi^3 + \sigma \nabla^2 \phi) + ab,
\end{aligned} \tag{A2}$$

where

$$\phi = \frac{2c - c_s - c_l}{c_s - c_l} \tag{A3}$$

such that $\phi = 1$ corresponds to the concentration of the precipitate and $\phi = -1$ corresponds to the concentration of C in the saturated liquid solution.

APPENDIX B: SOLUTIONS OF REACTION-DIFFUSION EQUATIONS WHEN $a_0 \neq 1$

We are analyzing the following RD equations:

$$\begin{aligned}\frac{\partial a}{\partial t} + \frac{Q}{r}\frac{\partial a}{\partial r} &= \frac{\partial^2 a}{\partial r^2} + \frac{1}{r}\frac{\partial a}{\partial r} - ab,\\ \frac{\partial b}{\partial t} + \frac{Q}{r}\frac{\partial b}{\partial r} &= \frac{\partial^2 b}{\partial r^2} + \frac{1}{r}\frac{\partial b}{\partial r} - ab\end{aligned} \tag{B1}$$

with the initial conditions

$$\begin{aligned}a(r > r_0, t = 0) &= 0,\\ b(r > r_0, t = 0) &= b_0,\end{aligned} \tag{B2}$$

and boundary conditions

$$\begin{aligned}a(r = r_0, t) = a_0, \quad \frac{\partial a}{\partial r}(r = R_{\text{tot}}, t) &= 0,\\ b(r = r_0, t) = 0, \quad \frac{\partial b}{\partial r}(r = R_{\text{tot}}, t) &= 0,\end{aligned} \tag{B3}$$

where R_{tot} is the radius of the domain.

Brau *et al.* [18] have studied the solutions of the same equations

$$\begin{aligned}\frac{\partial a^*}{\partial t^*} + \frac{Q^*}{r^*}\frac{\partial a^*}{\partial r^*} &= \frac{\partial^2 a^*}{\partial r^{*2}} + \frac{1}{r^*}\frac{\partial a^*}{\partial r^*} - a^* b^*,\\ \frac{\partial b^*}{\partial t^*} + \frac{Q^*}{r^*}\frac{\partial b^*}{\partial r^*} &= \frac{\partial^2 b^*}{\partial r^{*2}} + \frac{1}{r^*}\frac{\partial b^*}{\partial r^*} - a^* b^*,\end{aligned} \tag{B4}$$

but with initial conditions

$$\begin{aligned}a^*(r^* > r_0^*, t^* = 0) &= 0,\\ b^*(r^* > r_0^*, t^* = 0) &= \beta,\end{aligned} \tag{B5}$$

and boundary conditions

$$\begin{aligned}a^*({}^*r = r_0^*, t^*) = 1, \quad \frac{\partial a^*}{\partial r^*}(r^* = R_{\text{tot}}, t^*) &= 0,\\ b^*({}^*r = r_0^*, t^*) = 0, \quad \frac{\partial b^*}{\partial r^*}(r^* = R_{\text{tot}}, t^*) &= 0,\end{aligned} \tag{B6}$$

for which they have derived the following scaling laws:

$$r_f^* = 2\kappa^{1/2} t^{*1/2}, \tag{B7}$$

$$R^*(r_f^*, t^*) = \frac{29}{\pi^4} K_{\text{rad}}^{4/3} t^{*-2/3}, \tag{B8}$$

$$w^* = \pi K_{\text{rad}}^{-1/3} t^{*1/6}. \tag{B9}$$

Noticing that Brau *et al.*'s problem can be mapped to our model by the change of variables $a^* = a/a_0$, $b^* = b/a_0$, $t^* = t/a_0$, $r^* = r/a_0^{1/2}$, $Q^* = Q$, we get the scaling laws for the case where $a_0 \neq 1$:

$$r_f = 2\kappa^{1/2} t^{1/2}, \tag{B10}$$

$$\begin{aligned}R(r_f, t) &= \frac{29}{\pi^4}(a_0 K_{\text{rad}})^{4/3} t^{-2/3}\\ &= \frac{29}{\pi^4}\left(\frac{b_0 K_{\text{rad}}}{\beta}\right)^{4/3} t^{-2/3},\end{aligned} \tag{B11}$$

$$\begin{aligned}w &= \pi (a_0 K_{\text{rad}})^{-1/3} t^{1/6}\\ &= \pi \left(\frac{b_0 K_{\text{rad}}}{\beta}\right)^{-1/3} t^{1/6}.\end{aligned} \tag{B12}$$

A similar reasoning can be done for the rectilinear case.

APPENDIX C: SCALINGS OF THE FRONT FOR A SEMI-INFINITE RECTILINEAR GEOMETRY

Let us show explicitly that the coefficients of the scaling laws (27)–(29) computed for the radial geometry when $Q = 1$ can be used to determine the coefficients for the front in a semi-infinite rectilinear geometry. To do so, we revisit the 1D rectilinear case but in a semi-infinite system with a fixed boundary condition at $x = 0$. The differential equations are

$$\partial_t a = \partial_{xx} a - ab, \tag{C1}$$

$$\partial_t b = \partial_{xx} b - ab, \tag{C2}$$

with the initial condition $a(x, t = 0) = 0$ and $b(x, t = 0) = b_0$. The boundary condition on the left border is $a(x = 0, t) = a_0$ and $b(x = 0, t) = 0$ and we have at $x \to \infty$: $a = 0$ and $b = b_0$.

Let us first compute the coefficient of the position x_f of the front. Physically, the difference with the infinite system is that the constant feeding of reactant A at the origin can only induce $x_f \geqslant 0$, contrary to the infinite system where x_f can be both positive or negative depending on the initial concentrations and diffusion coefficients [17,38]. Defining $u = a - b$, and substracting (C2) from (C1), we get the equation for u:

$$\partial_t u = \partial_{xx} u, \tag{C3}$$

with the boundary conditions $u(0, t) = a_0$ and $u(\infty, t) = -b_0$. The solution is thus

$$u(x, t) = (a_0 + b_0) * \text{erfc}\left(\frac{x}{2\sqrt{t}}\right) - b_0. \tag{C4}$$

The position x_f is defined as the location where $a(x_f, t) = b(x_f, t)$ and thus $u(x_f, t) = 0$. From this, x_f can be found as a solution of the equation

$$(a_0 + b_0) * \text{erfc}\left(\frac{x_f}{2\sqrt{t}}\right) - b_0 = 0, \tag{C5}$$

which gives explicitly

$$x_f = 2\sqrt{t} * \text{erf}^{-1}\left(\frac{b_0}{b_0 + a_0}\right), \tag{C6}$$

$$= 2\sqrt{t} * \text{erf}^{-1}\left(\frac{1}{1 + \beta}\right) \tag{C7}$$

$$= \alpha_{\text{si}}(\beta)\sqrt{t}. \tag{C8}$$

This expression for $\alpha_{\rm si}(\beta)$ (where "si" stands for "semi-infinite") can be found with Eqs. (27)–(29), where $Q = 1$ because the coefficients $\alpha_{\rm si}(\beta)$ and $\alpha_{\rm rad}(\beta, 1)$ are solution of the same equation with the same boundary and initial conditions. This can be also recovered by starting from Eq. (27) where $Q = 1$:

$$r_f = \alpha_{\rm rad}(\beta, 1)t^{1/2} = 2\kappa^{1/2}(1, \beta)t^{1/2} \tag{C9}$$

$$= 2\left[\chi^{-1}\left(\frac{1}{2}, \frac{\beta}{1+\beta}\right)\right]^{1/2} t^{1/2}. \tag{C10}$$

Noting the property

$$\chi^{-1}\left(\tfrac{1}{2}, x\right) = [\mathrm{erf}^{-1}(1-x)]^2 \tag{C11}$$

we eventually find

$$r_f = 2\left[\mathrm{erf}^{-1}\left(1 - \frac{\beta}{1+\beta}\right)\right]t^{1/2} \tag{C12}$$

$$= 2 * \mathrm{erf}^{-1}\left(\frac{1}{1+\beta}\right) * \sqrt{t} = \alpha_{\rm si} t^{1/2}. \tag{C13}$$

Now that we have verified the equivalence, we can summarize the three scalings for the semi-infinite rectilinear reaction front from the radial one where $Q = 1$:

$$x_f = \alpha_{\rm si}(\beta)t^{1/2} \tag{C14}$$

$$= 2\,\mathrm{erf}^{-1}\left(\frac{1}{1+\beta}\right)t^{1/2}, \tag{C15}$$

$$R(x_f, t) = \xi_{\rm si}(\beta, b_0)t^{-2/3} \tag{C16}$$

$$= \frac{29}{\pi^4}\left(\frac{b_0 K_{\rm rad}(1, \beta)}{\beta}\right)^{4/3} t^{-2/3}, \tag{C17}$$

$$w = \delta_{\rm si}(\beta, b_0)t^{\frac{1}{6}} \tag{C18}$$

$$= \pi\left(\frac{b_0 K_{\rm rad}(1, \beta)}{\beta}\right)^{-1/3} t^{1/6}, \tag{C19}$$

where

$$K_{\rm rad}(1, \beta) = \frac{1+\beta}{\sqrt{\pi}} e^{\mathrm{erf}^{-1}\left(\frac{1}{1+\beta}\right)}. \tag{C20}$$

We see in particular via (C15) that, indeed, the front can only invade the reactant B, i.e., x_f can only be positive as the left boundary is constantly fed by reactant A. We can also deduce the value of $\langle \phi_{\rm lin}^{\rm si} \rangle$,

$$\left\langle \phi_{\rm lin}^{\rm si}(b_0, \beta) \right\rangle = \langle \phi_{\rm rad}(b_0, \beta, Q = 1) \rangle. \tag{C21}$$

[1] M. C. Cross and P. C. Hohenberg, Pattern formation outside of equilibrium, Rev. Mod. Phys. **65**, 851 (1993).

[2] G. Schuszter, F. Brau, and A. De Wit, Calcium carbonate mineralization in a confined geometry, Environ. Sci. Technol. Lett. **3**, 156 (2016).

[3] P. Damacet and K. A. Mirica, Periodic patterning of matter in non-equilibrium Liesegang-type structures, Angew. Chem. Int. Ed. **64**, e202425292 (2025).

[4] F. Haudin, J. H. E. Cartwright, F. Brau, and A. De Wit, Spiral precipitation patterns in confined chemical gardens, Proc. Natl. Acad. Sci. USA **111**, 17363 (2014).

[5] M. Itatani, Q. Fang, K. Unoura, and H. Nabika, Programmable design of self-organized patterns through a precipitation reaction, J. Phys. Chem. B **124**, 8402 (2020).

[6] Q. Wang and E. Nakouzi, Reaction-diffusion coupling facilitates the sequential precipitation of metal ions from battery feedstock solutions, Environ. Sci. Technol. Lett. **10**, 1188 (2023).

[7] B. Bohner, G. Schuszter, O. Berkesi, D. Horváth, and A. Tóth, Self-organization of calcium oxalate by flow-driven precipitation, Chem. Commun. **50**, 4289 (2014).

[8] I. Ziemecka, S. Gokalp, S. Stroobants, F. Brau, D. Maes, and A. De Wit, Polymorph selection of ROY by flow-driven crystallization, Crystals **9**, 351 (2019).

[9] B. A. Grzybowski and C. J. Campbell, Fabrication using programmed reactions, Mater. Today **10**, 38 (2007).

[10] P. Knoll, E. Nakouzi, and O. Steinbock, Mesoscopic reaction-diffusion fronts control biomorph growth, J. Phys. Chem. **121**, 26133 (2017).

[11] B. Bohner, G. Schuszter, D. Horváth, and A. Tóth, Morphology control by flow-driven self-organizing precipitation, Chem. Phys. Lett. **631–632**, 114 (2015).

[12] G. Schuszter and A. De Wit, Comparison of flow-controlled calcium and barium carbonate precipitation patterns, J. Chem. Phys. **145**, 224201 (2016).

[13] G. Facchini, M. A. Budroni, G. Schuszter, F. Brau, and A. De Wit, Phyllotactic structures in radially growing spatial symmetry breaking systems, Phys. Rev. Lett. **135**, 018001 (2025).

[14] E. Balog, P. Papp, A. Tóth, D. Horváth, and G. Schuszter, The impact of reaction rate on the formation of flow-driven confined precipitate patterns, Phys. Chem. Chem. Phys. **22**, 13390 (2020).

[15] Y. Nagatsu, Y. Ishii, Y. Tada, and A. De Wit, Hydrodynamic fingering instability induced by a precipitation reaction, Phys. Rev. Lett. **113**, 024502 (2014).

[16] E. Balog, K. Bittmann, K. Schwarzenberger, K. Eckert, A. De Wit, and G. Schuszter, Influence of microscopic precipitate structures on macroscopic pattern formation in reactive flows in a confined geometry, Phys. Chem. Chem. Phys. **21**, 2910 (2019).

[17] L. Gálfi and Z. Rácz, Properties of the reaction front in an $A + B \to C$ type reaction-diffusion process, Phys. Rev. A **38**, 3151 (1988).

[18] F. Brau, G. Schuszter, and A. De Wit, Flow control of $A + B \to C$ fronts by radial injection, Phys. Rev. Lett. **118**, 134101 (2017).

[19] Y. Stergiou, D. M. Escala, P. Papp, D. Horváth, M. J. B. Hauser, F. Brau, A. De Wit, A. Tóth, K. Eckert, and K. Schwarzenberger, Unraveling dispersion and buoyancy dynamics around radial $A + B \to C$ reaction fronts: Microgravity experiments and numerical simulations, npj Microgravity **10**, 53 (2024).

[20] Y. Stergiou, M. J. B. Hauser, A. Comolli, F. Brau, A. De Wit, G. Schuszter, P. Papp, D. Horváth, C. Roux, V. Pimienta,

K. Eckert, and K. Schwarzenberger, Effects of gravity modulation on the dynamics of a radial $A + B \rightarrow C$ reaction front, Chem. Eng. Sci. **257**, 117703 (2022).

[21] R. Matalon and A. Packter, The Liesegang phenomenon. I. Sol protection and diffusion, J. Colloid Sci. **10**, 46 (1955).

[22] S. K. Smoukov, A. Bitner, C. J. Campbell, K. Kandere-Grzybowska, and B. A. Grzybowski, Nano- and microscopic surface wrinkles of linearly increasing heights prepared by periodic precipitation, J. Am. Chem. Soc. **127**, 17803 (2005).

[23] A. Sahu, B. B. Kanrar, and D. Panda, Evolution of micron-spaced patterns within precipitating patterns of in situ synthesized silver nanoparticles in a nanodot-embedded PVA/PVP film, Langmuir **37**, 4460 (2021).

[24] H. Nabika, M. Itatani, and I. Lagzi, Pattern formation in precipitation reactions: The Liesegang phenomenon, Langmuir **36**, 481 (2020).

[25] T. Antal, M. Droz, J. Magnin, and Z. Rácz, Formation of Liesegang patterns: A spinodal decomposition scenario, Phys. Rev. Lett. **83**, 2880 (1999).

[26] I. Lagzi, A. Volford, and A. Büki, Effect of geometry on the time law of Liesegang patterning, Chem. Phys. Lett. **396**, 97 (2004).

[27] M. Dayeh, M. Ammar, and M. Al-Ghoul, Transition from rings to spots in a precipitation reaction-diffusion system, RSC Adv. **4**, 60034 (2014).

[28] F. Izsák and I. Lagzi, A new universal law for the Liesegang pattern formation, J. Chem. Phys. **122**, 184707 (2005).

[29] P. Papp, B. Bohner, A. Tóth, and D. Horváth, Fine tuning of pattern selection in the cadmium-hydroxyde system, J. Chem. Phys. **152**, 094906 (2020).

[30] H. Wu, A review on the Cahn-Hilliard equation: Classical results and recent advances in dynamic boundary conditions, Electron. Res. Arch. **30**, 2788 (2022).

[31] F. Brau and A. De Wit, Influence of rectilinear vs radial advection on the yield of $A + B \rightarrow C$ reaction fronts: A comparison, J. Chem. Phys. **152**, 054716 (2020).

[32] W. van Saarloos, Front propagation into unstable states, Phys. Rep. **386**, 29 (2003).

[33] S. M. Tuur, A. M. Nelson, D. W. Gibson, R. C. Neafie, F. B. Johnson, F. K. Mostofi, and D. H. Connor, Liesegang rings in tissue. How to distinguish Liesegang rings from the giant kidney worm, dioctophyma renale, Am. J. Surg. Pathol. **11**, 598 (1987).

[34] T. S. Babicheva, A. A. Konduktorova, S. L. Shmakov, and A. B. Shipovskaya, Formation of Liesegang structures under the conditions of the spatiotemporal reaction of polymer-analogous transformation (salt-base) of chitosan, J. Phys. Chem. B **124**, 9255 (2020).

[35] R. M. Walliser, F. Boudoire, E. Orosz, R. Tóth, A. Braun, E. C. Constable, Z. Rácz, and I. Lagzi, Growth of nanoparticles and microparticles by controlled reaction-diffusion processes, Langmuir **31**, 1828 (2015).

[36] C. Campbell, E. Baker, M. Fialkowski, and B. Grzybowski, Arrays of microlenses of complex shapes prepared by reaction-diffusion in thin films of ionically doped gels, Appl. Phys. Lett. **85**, 1871 (2004).

[37] U. Thiele, T. Frohoff-Hülsmann, S. Engelnkemper, E. Knobloch, and A. Archer, First order phase transitions and the thermodynamic limit, New J. Phys. **21**, 123021 (2019).

[38] Z. Koza, The long-time behavior of initially separated $A + B \rightarrow 0$ reaction-diffusion systems with arbitrary diffusion constants, J. Stat. Phys. **85**, 179 (1996).